# Variational methods for shape modelling

## Summary of the PhD Thesis
### by

## Csaba Molnár

Supervisors:

### Peter Horvath
### Zoltan Kato

Doctoral School of Computer Science

Institute of Informatics
University of Szeged

Biological Research Centre of Hungarian
Academy of Sciences in Szeged

Szeged
2019

# 1 Introduction

Unprecedented advances in gathering and storing digital information have fuelled the need for computer-based, fast and reliable processing of digital images to explore meaningful information from these complicated and heterogeneous image data. For example, in life sciences, advancements in microscopy offer novel opportunities for a never-seen in-depth and detailed analysis of biological systems, however, exploring this plethora of information requires an automated processing of tens of thousands of images. Image segmentation is a key first step of image processing, during which visual objects (regions, shapes) are extracted from the images. However, efficient and precise image segmentation often requires prior knowledge on the objects in the images. Our research has focused on the development of novel image segmentation algorithms that exploit the objects' shape characteristics as a priori knowledge. During the development of these new segmentation algorithms, we aimed to preserve the original morphologies of the objects present in the images, as morphology often carries key information on the object itself. Taking these criteria into consideration, we have developed several variational methods which are suitable to segment an unknown number of objects with well-defined morphological characteristics present in the image. We focused on analysing images where the objects are densely packed.

# 2 Preliminaries: higher-order active contours and phase field models for shape modelling

*Variational methods* are widely used in computer vision applications. *Active contour* models are an important family of this variational approach. They can yield closed object boundaries as a result of segmentation. In this approach the representation of the boundary of the object of interest is a chain of points over the image space. The points of this chain, or the *curve*, are forced to move during the optimization process driven by internal and external forces. The internal energy comes from the curve itself, while the external energy is derived from the image.

A fast numerical algorithm has been proposed for active contours, but for closed curves it does not allow changes of topology, since the final curve has the same topology as the initial one. To overcome the limitation of the changes of topology, Osher and Sethian [1] proposed the *level set method,* where the curve is implicitly represented by a higher dimensional function (see also in [2, 3]). This level set function $\phi$ represents the closed curve $\mathbf{r}$ as a zero-level set of $\phi$: $\mathbf{r} = \{(x,y)|\phi(x,y) = 0\}$.

*Phase field model* is a mathematical model for solving interfacial problems. In image processing applications, it can be utilized as a special level set modelling technique that has advantages over classical level set models. No special initial configuration is required for the optimization process; no reinitialization or regularization steps are needed, and thus the process of finding the solution is faster.

*Higher-order active contour* (HOAC) models [4] provide a templateless approach to express shape information. HOAC models can describe shape priors using long-range dependencies between region boundary points. The long-range interaction is expressed by a multiple integral over the boundary contour. In the simplest case of a HOAC model, the contour energy is composed of area and perimeter minimizer

1

terms, and extended by a double integral over the boundary points. This higher-order term competes with the minimizer terms resulting in various preferred shapes, such as network-like structures [4]. To extract tree crowns in aerial images, Horvath et al. [5] have proposed a special parametrization of the HOAC model, the 'gas of near-circles' (GOC) model which prefers circular objects.

Rochery et al. [6] have introduced a phase field model that is equivalent to the HOAC models (*i.e.* sophisticated prior geometric knowledge can be included while maintaining the advantages of the phase field models). The simple higher-order phase field energy is be formulated as:

$$
E_{f,g}(\phi) = \int_\Omega \left\{ \overbrace{\frac{D_f}{2}|\nabla\phi|^2 + \underbrace{\alpha_f\left(\phi - \frac{\phi^3}{3}\right) + \lambda_f\left(\frac{\phi^4}{4} - \frac{\phi^2}{2}\right)}_{V}}^{E_{f,0}} \right\}
$$
$$
- \frac{\beta_f}{2} \iint_{\Omega\times\Omega'} \nabla\phi\, \mathbf{G}(x,x')\, \nabla\phi' \, , \tag{1}
$$

where (un)primed functions are evaluated at $(x \in \Omega)$ $x' \in \Omega' \equiv \Omega$. The interaction function $\mathbf{G}(x,x') = \Psi(|x - x'|)\mathbf{I}$, where $\mathbf{I}$ is the $2 \times 2$ unit matrix.

Horvath et al. [7] have described the conversion of the parameters of the HOAC GOC model to the phase field GOC model.

# 3 Multi-layered 'gas of near-circles' phase field model

The GOC model, whether in its active contour or phase field formulation, has two main limitations. The first one comes from the representation: like most segmentation methods, it cannot represent overlapping objects since the solution is given as a partitioning of the image domain into disjoint regions. The second limitation arises from the geometric model itself: the non-local energy term, which causes the model to favour near-circular shapes, also results in a repulsive force between neighbouring objects separated by a distance comparable to the desired object size. To overcome these limitations, we have introduced an extension of the presented GOC method in which we have successfully eliminated all the above-mentioned weaknesses.

We have extended the single-layered phase field model of Eq. (1) to a *multi-layered* GOC phase field model (MLGOC) [8]. Using multiple instances of the classical models enables the representation of not only disjoint subsets, but also sets of subsets of the image domain possibly having non-empty intersection, which can now be represented on separate layers (see Fig. 1). Formally it means that the definition of segmentation needs to be changed slightly: the condition which prevents two different regions from having common pixels, can be omitted. As a result, the new model is able to represent objects that touch and overlap in the image.

Moreover, the long-range interaction of the GOC model creates a repulsion between connected components. This repulsive force favours configurations in which the objects are separated by a distance comparable to their size. While it is appropriate for some tasks, *e.g.* tree crowns in regular plantations [7], it fails in solving
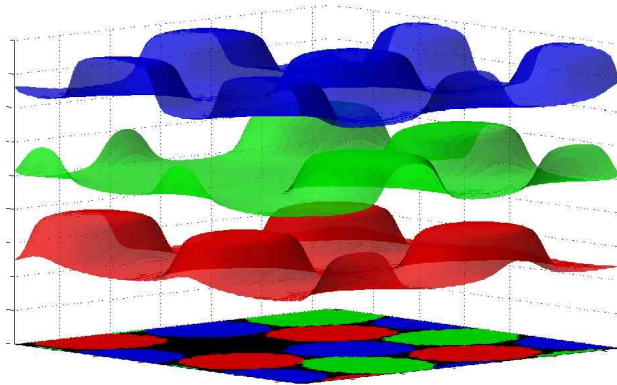
Figure 1: Multi-layered 'gas of near-circles' (MLGOC) phase field model. Three surfaces illustrate a stable configuration of the MLGOC model. Under the surfaces there is the corresponding segmentation. Positive overlap penalty forces the segmented regions to move in positions where they overlap with no regions from other layers.

problems in which objects are touching or overlapping. To avoid this limitation, in the new model the long-range interactions act intra-layer but *not* inter-layer [8]. This has two effects. First, the low-energy configurations in each layer are still 'gas of near-circles' configurations, as required. Second, the repulsive interaction is eliminated, because repulsively interacting regions can exist on separate layers. The result is that overlapping 'gas of near-circles' configurations on separate layers can now be combined without penalty (Fig. 2). However, to avoid degenerate configurations, in which a given object is duplicated across all layers, an inter-layer area overlap penalty was introduced [8].

To proceed, we redefined the phase field as a multi-component object: $\Phi = \{\phi^{(i)}\}_{i \in [1..\ell]} : [1..\ell] \times \Omega \to \mathbb{R}$, where $\ell$ is the number of layers. The total energy $\tilde{E}_f$ of the new multi-layered model then takes the form

$$\tilde{E}_f(\Phi) = \sum_{i=1}^{\ell} E_{f,g}(\phi^{(i)}) + \frac{\kappa_O}{4} \sum_{i \neq j} \int_{\Omega} (1 + \phi^{(i)})(1 + \phi^{(j)}) \,, \qquad (2)$$

where $E_{f,g}$ is defined in Eq. (1), and $\kappa_O$ is a new parameter controlling the strength of the overlap penalty.

Here are some observations about the effect of overlap penalty:

- As expected, $\kappa_O = 0$ yields overlapping objects, while $\kappa_O > 0$ prevents overlaps (see Fig. 2).

- From Eq. (2), 'background' points, with $\phi^{(i)} \simeq -1$, do not generate overlap penalty.

- If they do not overlap, objects in the range of the repulsive interaction will tend to lie in different layers.

- If they do overlap, there is competition between the repulsive interaction and the overlap penalty.

3

- If $\kappa_O$ is not too large, they will exist on separate layers; if $\kappa_O$ is large enough, they will exist on the same layer, perhaps merging to one object.

- If $\kappa_O$ is too high, then either an empty configuration or unstable circles are produced.
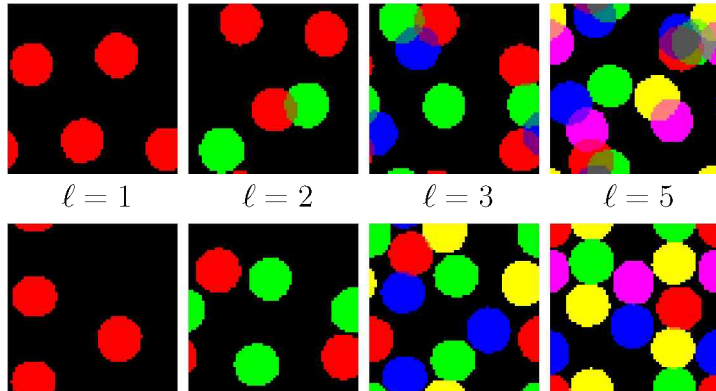


Figure 2: Typical configurations of the prior model ($r_0 = 10$, negative circle energy) using different number of layers ($\ell$). The weight of overlap penalty $\kappa_O = 0$ in the top row and $\kappa_O = 0.02$ in the bottom row.

Fig. 2 shows some minimum energy configurations of the prior model.

## 3.1   Combination with image data

In our tests we have used a likelihood energy with the following assumptions: first, the foreground and background pixel intensities follow two different normal distributions which can be calculated by maximum likelihood estimation; second, high image gradient can be measured between the foreground and background intensities. This is the case when the resolution is not high enough to resolve the texture of foreground of the objects [5] (*e.g.* some types of lipid droplets of the size of a few microns with resolution $\sim 0.4$ $\mu$m). We used the following phase field data term paired with each $\phi^{(i)}$ layer:

$$E_I(I, \phi^{(i)}) = \int_\Omega \left\{ \gamma_1 \nabla I \cdot \nabla \phi^{(i)} + \gamma_2 \left[ \frac{(I - \mu_{\text{in}})^2}{2\sigma_{\text{in}}^2} \phi_+^{(i)} + \frac{(I - \mu_{\text{out}})^2}{2\sigma_{\text{out}}^2} \phi_-^{(i)} \right] \right\}, \quad (3)$$

where: $\nabla \phi^{(i)}$, and $\phi_\pm^{(i)} = (1 \pm \phi)/2$ are approximately the normal vector to the boundary, and the characteristic functions of the region $(+)$ and its complement $(-)$, respectively [7]; $I : \Omega \to \mathbb{R}$ is the image data; $\mu_{\text{in,out}}$ and $\sigma_{\text{in,out}}$ are the parameters of pixel-wise Gaussian distributions modelling the image in the interior (in) and exterior (out) regions, learned from samples; and $\gamma_{1,2}$ are positive weights.

## 3.2   Computational complexity

A significant advantage of using level sets or phase fields for representation of active contour models is that the density of the information in the image (*i.e.* the number

of objects) does not increase the computational complexity of the model. Since the segmented regions are uniquely defined by the level set and a given threshold at any point of its evolution, the increasing number of segmented objects have no unwanted effects on the computing costs of evolution. Of course in our new model we use the term multi-layered model, and therefore the amount of operations required is multiple compared to the single-layered model. The computational time increases linearly with the number of phase field layers used. Experience has shown that a maximum of 4 layers is usually enough to properly handle configurations of even the highest density.

# 4 Additive data model for fluorescent microscopy

Recently, both the academic and the industrial sectors have been increasingly interested in developing more complex three-dimensional cell culture models. These can better capture the complexity of the tissue, and have the potential to provide more relevant biological information compared to the traditional two-dimensional models [9, 10, 11]. Upon transforming the imaging of such models into simple 2D images, several situations may arise when the objects (cells) of interest overlap (Fig. 3).
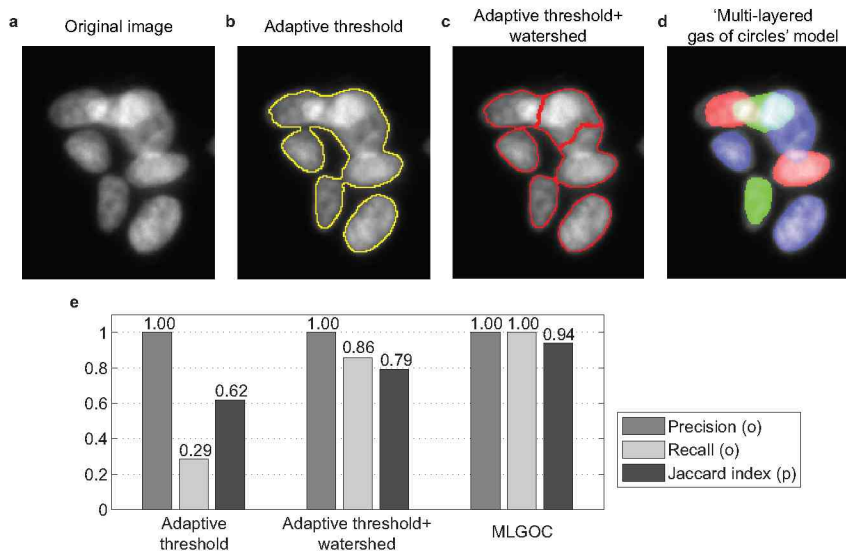


Figure 3: Comparison of different methods on microscopic images containing overlapping cells. Top row from left to right: (a) Original image; (b) Results (Region of Interest) obtained by adaptive Otsu thresholding (c) Results of the standard watershed segmentation method; (d) Results with the proposed 'multi-layered gas of near-circles' method; (e) Precision, recall and Jaccard index of segmented objects ('o' and 'p' indicate that the metrics are computed at the object and pixel level, respectively).

The point spread function (PSF) plays an important role in the image formation theory of the (fluorescent) microscope. The PSF of an optical device is the image of a single point object (rescaled to make its integral all over the space equal 1). This is mathematically represented by a convolution equation:

$$I(x,y) = O * PSF = \iint O(u,v)PSF(x-u, y-v)dudv \ , \tag{4}$$

where $O(u, v)$ is the intensity of the emitted light of the particle at position $(u, v)$; $PSF : \mathbb{R}^3 \to \mathbb{R}$ is the point spread function of the microscope. It gives that the measured intensities of the acquired image are proportional to the number of the fluorophores in the range of PSF.

## 4.1 Image formation model and image data model for overlapping cell nuclei

The image formation model we used is $I_{\text{observed}} = I_{\text{background}} + I_{\text{original}}$. $I_{\text{background}}$ is a nearly flat non-zero surface with noise, so-called 'dark noise'. Let $\mu_-$ and $\sigma_-^2$ be the mean and variance of the background intensity, and $\mu_+$ and $\sigma_+^2$ be the mean and variance of the measured intensity of a single cell. Let $\Delta\mu = \mu_+^2 - \mu_-^2$, and $\Delta\sigma^2 = \sigma_+^2 - \sigma_-^2$. Then, according to the model, the mean of the intensity of multiple $(n)$ cells is given by $\mu_- + n\Delta\mu$ , and its variance by $\sigma_-^2 + n\Delta\sigma^2$. The parameters $\mu_-$, $\sigma_-^2$, $\Delta\mu$, and $\Delta\sigma^2$ were estimated from the corrected images using maximum likelihood estimation.

We have introduced a new data model which is adapted to the image formation process in fluorescent imaging. The new model is constructed by using the assumption that overlapping cells additively contribute to pixel intensities of the acquired image, so that multiple cells on top of each other produce an intensity contribution which is a multiple of that of a single cell.

Let $\phi_+ = \sum_{i=1}^{\ell} \frac{(\tanh(\phi^{(i)})+1)}{2}$ (Fig. 4), where $\phi^{(i)}$ is the phase field in the $i^{\text{th}}$ layer; this quantity 'counts' the number of cells at each point. Let $\gamma_d$ be the (positive) weight of the data term; and let $I$ be the intensity of the input image. Using the image formation model described earlier, and a Gaussian model for the image noise, the new data term becomes [12]:

$$E_{\text{intensity}}(I, \phi_+) = \gamma_d \int_\Omega \frac{(I - \mu_- - \Delta\mu\phi_+)^2}{2(\sigma_-^2 + \Delta\sigma^2\phi_+)} dx . \tag{5}$$

Since a phase field takes the values -1 and 1 in its two stable phases of the energy potential (background and foreground), with a smooth transition between them, the integrand in Eq. (5), which is the energy density, takes a low value when $\phi_+ = 0$ over regions with background intensity; $\phi_+ = 1$ over regions of single-cell intensity; and generally, when $\phi_+ = n$ over regions with $n$ cell intensity.

## 4.2 Verification

In order to measure the robustness of the proposed method, we have generated data sets of synthetic images with different values for the noise variance, the extent of overlap, as well as with varying object ellipticity and size, to create variability similar to that seen in real world observations [13]. The proposed model was able to select circles with the desired radius and correctly separate overlapping objects, while at the same time eliminated the circles with smaller radius (see Fig. 4c). The proposed method was able to segment overlapping circles up to 0 dB with minimal error, with the first errors appearing at SNR = -5 dB. We have to note that the optimal data weight $\gamma_d$ depends on the level of the noise we have artificially added to the raw synthetic images. This dependency should come from the weighting role of the denominator in Eq. (5). The proposed method is suited to most conventional cell
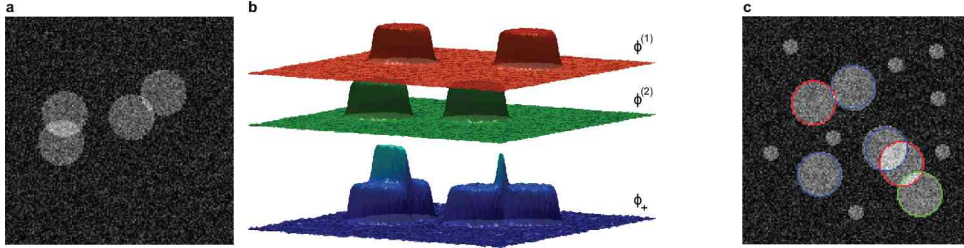
Figure 4: Illustration of the proposed data model and behaviour of the geometric model. (a) Noisy synthetic image. (b) Phase field representation of the cell configuration in the image (a), showing the two layers, and the combined $\phi_+$ function that 'counts' cells. (c) Size selectivity of the MLGOC model: using proper settings of the prior and data parameters, it is possible to achieve size-selective segmentation. No initial object seeds were used.

nuclei types, but we do not recommend its use when the major/minor $(r_{max}/r_{min})$ axis ratio exceeds 1.75. The segmentation results show that the accuracy is independent of the extent of the overlap, and that the method is capable of segmenting circles successfully.

# 5   Selective active contours

The main concept behind the construction of 'selective active contours' is to describe a wide family of shapes such as circles, ellipses or plasma-like shapes by simple descriptors such as area or/and perimeter, which can be effectively calculated by line integrals over the contour.

Here we give a novel geometric active contour representation of commonly used shape descriptors. From the huge number of shape descriptors we can select a few ones which cost a linear number of operations, *e.g.* circularity or some of the moments. We defined some very simple energy functionals as internal forces of curves, which functionals can model contours of specific shapes such as ellipsoids or plasma-like shapes. To keep our optimization numerically and topologically stable we have built smoothness terms into our shape functional.

## 5.1   Parts of composite functional

Next we will give a few possible options for the terms that prefer certain object size and shape. To promote a given perimeter we can give the error functional as

$$\mathcal{E}_{S-L}\left(\dot{\mathbf{r}}\right) = f_S\left(\oint ds - L_0\right) , \tag{6}$$

where $L_0$ is the preferred length of the object boundary, $ds = |\dot{\mathbf{r}}|dt$ and $f_S$ is the function having inflection at zero; a simple, practical choice with horizontal tangent line at the inflection point can be $f_S\left(x\right) = \frac{1}{3}x^3$. Similarly, characterizing objects with preferred internal area, the error functional is

$$\mathcal{E}_{S-A}\left(\mathbf{r}, \dot{\mathbf{r}}\right) = f_S \left( \oint dA - A_0 \right), \tag{7}$$

where $A_0$ is the preferred internal area of the object, $dA = \frac{1}{2}\mathbf{k} \cdot (\mathbf{r} \times \dot{\mathbf{r}})\, dt$ is the Euclidean area element, $\mathbf{k}$ is the normal of the plane of the (planar) curve $\mathbf{r}(t)$.

Note that using these functions, the inflection point can be easily extended to 'inflection range' to select objects with sizes falling between two threshold limit values.

Further selectivity can be achieved by adding shape prior to the functional. Various features have been designed to represent shapes that are based either on information about shape boundary or on boundary plus interior region. Any contour or region based global shape descriptor can be incorporated into the energy minimization methods [14]. Here we present two contour based priors inflicting the least possible computation load. The ratio of the square of the object's perimeter and the enclosed area $q_C = \frac{\left(\oint ds\right)^2}{\oint dA}$ is being used as the simplest global shape descriptor to distinguish objects with elongated parts from compact ones. The simplest functional penalizes the deviation from the ratio $q_C$ is defined by the function $f_{SH}$ as

$$\mathcal{E}_{SH-C}\left(\mathbf{r}, \dot{\mathbf{r}}\right) = f_{SH}\left( \oint dA - \frac{1}{q_C}\left(\oint ds\right)^2 \right) \tag{8}$$

with minimum at zero.

The central moments of the enclosed area or contour itself are often used as well. The normalized second central moment of the contour $\frac{1}{q_M} = \frac{M_2}{\oint dA \oint ds}$ (where $M_2 = \oint |\mathbf{r}_{0t}|^2\, ds$, $\mathbf{r}_{0t} = \mathbf{r} - \mathbf{r}_0$ and $\mathbf{r}_0$ is the center of gravity of the contour: $\mathbf{r}_0 = \frac{\oint \mathbf{r}\, ds}{\oint ds}$ ) has strong shape discrimination effect and can also be calculated along the contour with line integral. The functional penalizing the deviation from a preferred normalized second moment is:

$$\mathcal{E}_{SH-M}\left(\mathbf{r}, \dot{\mathbf{r}}\right) = f_{SH}\left( \oint dA \oint ds - q_M M_2 \right). \tag{9}$$

Similarly to the size prior, the minimum point can be extended to a minimum range to select minimizer shapes falling between threshold limit values.

To get a stable solution, the combination of the size and shape priors require a smoothness term to be added.

For the smoothness term we use $\kappa^2$ ($\kappa = \frac{\ddot{\mathbf{r}} \cdot \mathbf{n}}{|\dot{\mathbf{r}}|^2}$), which has a well defined meaning originating from the mechanics of the flexible rods: the bending energy of the curve called 'Euler elastica' [15]. The smoothness based on this quantity is:

$$\mathcal{E}_{SM-EE}\left(\dot{\mathbf{r}}, \ddot{\mathbf{r}}\right) = \frac{1}{2} \oint \kappa^2 ds. \tag{10}$$

This smoothness term has minimal interference with the other terms, however, for contours with small size, it predisposes to display over-smoothing effect, preferring circles over elongated objects.

The use of integral terms with different dimensions would require different weights between the terms in both the internal and external forces depending on the size of

the objects. From a theoretical point of view, using dimensionless terms in the composite functional would be the most appropriate solution, however, this can rarely be achieved without compromising the overall performance of the methods. Fortunately, in most cases, a simpler approach (normalizing by a function of the targeted area and/or length) provides an acceptable result. The three component functionals, including the size, the shape and the smoothness terms, can be combined such that their internal weights are fixed once and for all.

## 5.2   Region based data term

To complete the classical active contour framework, we give a region based image model as the external part of the energy. Region based image models [16, 17, 18] have advantages over gradient- or edge-based data terms: a) they are proved to be very efficient in dealing with noisy images, and b) they are less sensitive to the initialization of the contours.

In our data model we define two local regions along the contour given by the Cartesian products of the local coordinates (see Fig. 5): $\mathfrak{R}^+ : \xi \in [-p, p] \times \eta \in [0, q]$, $\mathfrak{R}^- : \xi \in [-p, p] \times \eta \in [-q, 0]$. The segmentation problem is then represented by the intensity mean difference function expressed with local integrals

$$\Phi\left(\mathbf{r}, \mathbf{n}\right) = \frac{1}{\|\mathfrak{R}\|} \left( \iint_{\mathfrak{R}^+} I\left(\mathbf{p}\right) dA - \iint_{\mathfrak{R}^-} I\left(\mathbf{p}\right) dA \right) , \tag{11}$$

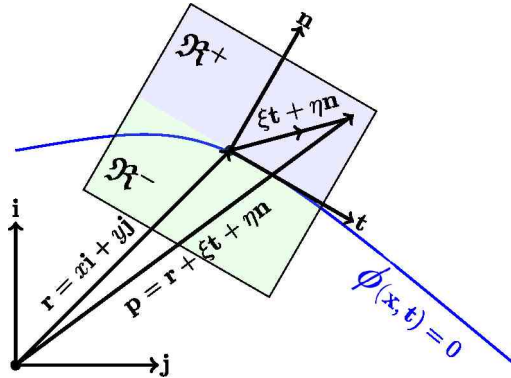where $dA = d\xi d\eta$, and $\|\mathfrak{R}\| = 2pq$.



Figure 5: The local coordinate system. Its abscissa is aligned with the tangent vector of the contour.

# 6   Object splitting active contours

In many biological applications cells have a non-uniform spacial distribution. From the practical (image processing) point of view, it means that upon exceeding a certain density of cells, the classical segmentation methods do not give single, separated cells, but rather groups of touching objects/cells. To analyze individual objects, further processing is required, which can separate the clumped objects.

We introduce the 'cutting arms' higher-order active contour model for splitting aggregated objects which are not distinguishable based on image information only.

The assumption behind the idea is that it is possible to identify dents on the object groups' boundary when two adjacent cells are touching. Thus, by connecting opposite dents, *i.e.* the concave points of the boundary of object groups, one can designate the border line between two adjacent cells. To 'connect' the elements of these opposite point pairs we have developed a higher-order active contour model (HOAC).

As it was presented previously, HOAC models are able to describe nonlocal interactions between distant points of the object boundary. This ability makes it possible to add shape information to the classical energy of the active contour models without using any template shapes of the target objects. It can also provide a tool for object splitting in the form of an attractive force between the contour points which satisfy certain properties, namely (1) they are not too far from each other, (2) they are aligned, and (3) they are concave points of the contour.

First, we assume that the set of objects that compose the clump of nuclei cannot be further segmented by using the method of presegmentation due to missing edge information between the parts. The splitting functional should therefore be based on purely geometric information. Second, we reduce the set of contour points to a subset satisfying certain concavity and alignment criteria. We call it 'feasible subset'. The complement set of the 'feasible subset' remains intact during the process. The feasible contour points are handled as a weighted, oriented particle set.

The associated orientation is defined by their normal vector $\mathbf{n}$, and the weights are defined by their concavity as shown in Fig. 6. Within an energy minimization framework for curve evolution, concavity is indicated by the negative curvature of the curve ($\kappa < 0$). The alignment of two oriented points (indexed by 1, 2) is defined by the relation of their orientations and relative position such that $a_{12} = \mathbf{n}_1 \cdot \mathbf{e}_{12} + \mathbf{n}_2 \cdot \mathbf{e}_{21}$, where $\mathbf{e}_{12}$ is the unit normal vector pointing from point 1 to 2, and $\mathbf{e}_{21} = -\mathbf{e}_{12}$. Note that this definition of the alignment is symmetric, *i.e.* $a_{12} = a_{21}$. Now one can define the 'anisotropic energy' for a pair of points as $U_{12} = f_c(\kappa_1) f_c(\kappa_2) g_a(a_{12}) l(d_{12})$ with $d_{12}$ being the Euclidean distance between the points and $f_c$, $g_a$, $l$ are appropriately chosen functions.
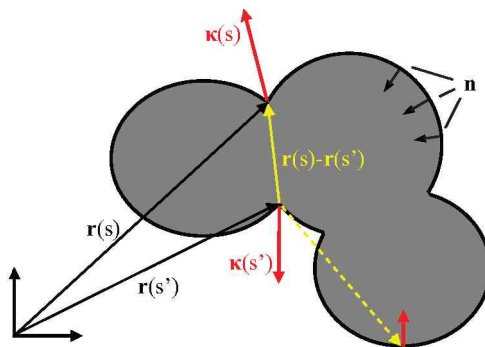


Figure 6: Illustration of the object cutting method. Contour points connected by the continuous line are well aligned, whilst points connected by the dashed line are not.

Taking $f_c(\kappa(s))$ as the density of the potential source along the contour, the second-order functional

$$E_{CA} = -\iint_{\mathbf{r}_{FS} \times \mathbf{r}'_{FS}} f_c\left(\kappa\left(s\right)\right) f_c\left(\kappa\left(s'\right)\right) g_a\left(a\left(s,s'\right)\right) l\left(d\left(s,s'\right)\right) ds\, ds' \qquad (12)$$

represents the total energy of the contour. The integral is evaluated only on the feasible subset, defined as:

$$\mathbf{r}_{FS} = \left\{ \mathbf{r}\left(s\right) \mid \kappa\left(s\right) < -\varepsilon \wedge a\left(s,s'\right) > \delta \right\} . \qquad (13)$$

We demonstrate the behaviour of the geometric model on different initial group of shapes (Fig. 7).
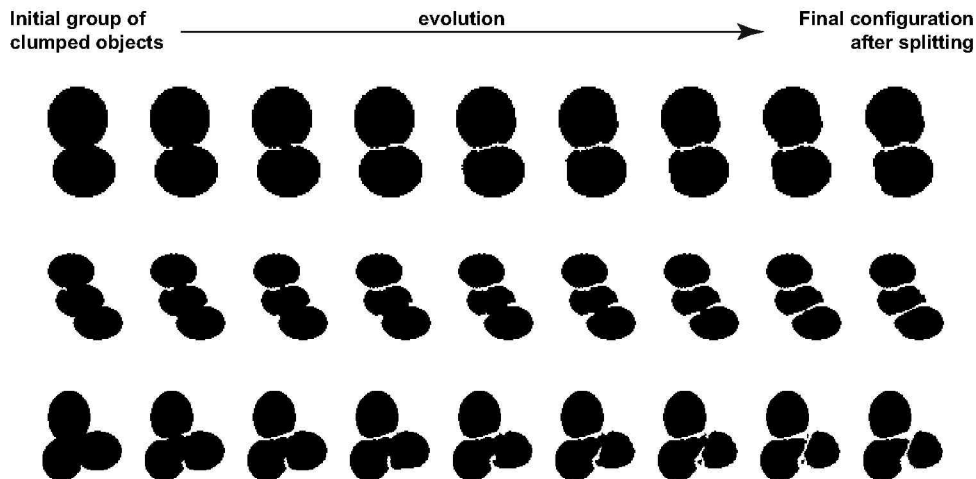


Figure 7: Behaviour of the geometric splitting model on different initial shapes.

# 7 Applications

The developed variational shape models were designed to solve segmentation tasks in challenging scenarios of high-throughput screening applications [19]. The models have been successfully used as a starting step of several real high-throughput experiments [19, 20, 21].

Our current understanding of biology is built upon population-averaged measurements. However, a growing number of studies indicate that heterogeneities of small subpopulations may carry important consequences for the entire population. For example, genetic heterogeneity plays a crucial role in drug resistance and the survival of tumours. To better understand biological systems with cellular heterogeneity, we increasingly rely on single-cell molecular analysis methods. However, single-cell isolation, the process by which we target and collect individual cells for further analysis is still technically challenging and lacks a perfect solution. We have developed a technique to increase the accuracy and throughput of microscopy-based single-cell isolation by automating the target selection and isolation process [20]. Computer-assisted microscopy isolation (CAMI) combines image analysis algorithms, machine learning, and high-throughput microscopy to recognize individual cells in suspensions or tissue, and automatically guide extraction through laser capture microdissection or micromanipulation. The MLGOC model combined with the new additive

model have had an important role in the elaboration of this single cell isolation system. To avoid contamination for further single-cell molecular analysis, the MLGOC model was used to filter out overlapping cells different from the target cell types. The CAMI system is capable of the isolation of thousands of single cells targeted upon phenotype and location characteristics.

# Summary and thesis points

In the following a listing of the key results of this dissertation are given. Table 1. summarizes the connection between the thesis points, their applications and the corresponding publications. The main findings of this research can be divided into three thesis groups.

In the first thesis group, I have presented a multi-layered variational model for segmentation of touching or overlapping objects in highly dense scenarios. The results were published in two conference proceedings [8, 12] and one journal paper [13].

I/1. I have created a synthetic image database containing images with circular objects of varying size and varying degree of additive noise. I have experimentally confirmed that the multi-layered 'gas of near-circles' phase field model (MLGOC), supplemented with a suitable data term, is capable of efficiently extracting touching or overlapping near-circular objects, described by the geometric model. In addition, I have experimentally demonstrated that the model is able to provide correct segmentation with several model parameter settings, even when starting from random initial conditions. This model has since been successfully applied for the segmentation of different types of biological images (microscopy images containing a large number of touching or partially overlapping cells or lipid droplets).

I/2. I have investigated and described how the new inter-layer phase field energy term, which controls the interaction between the independent layers, affects the behaviour of the geometric model. This term penalizes the overlap of objects from different layers, and therefore, helps to avoid degenerate solutions containing fully overlapping objects. Through simulations, I have analyzed the geometric model by sweeping through the layer number and penalty weight parameter spaces. Through these simulations, I have successfully demonstrated that the multi-layered model allows for better coverage of the image space compared to the original single-layer model, and thereby, it is capable to segment configurations of higher density. I have tested the model on large-scale synthetic data sets and I have demonstrated that an ideal weight of the overlap penalty term can be selected for a fixed data weight, such that the optimal segmentation can be achieved.

I/3. I have introduced an additive data model for the MLGOC phase field model, which is suitable for the segmentation of overlapping objects in fluorescent microscopy images. This new data model is capable of analyzing overlapping objects in fluorescent microscopy images, in which the measured intensity of overlapping objects is an additive function of the intensities of single objects. In order to measure the robustness of the proposed method, I have generated datasets of synthetic images to create a variability similar to that seen in real

world observations. I have experimentally verified that the combination of the MLGOC model and the additive data model shows high robustness against noise, shape deformations, initialization and the level of overlap of the objects. I have elaborated an algorithm for the effective initialization of the phase field layers in the multi-layered phase field model to improve segmentation results, as well as to reduce the number of layers and the iterations required.

In the second thesis group, I have presented a new family of active contours for an effective, size- and shape-selective segmentation. The results were published in a conference proceedings [22].

II/1. I have implemented an effective level set representation of the selective active contour model. All of the suggested shape descriptors have been given using simple line integrals over the objects' boundary. By simulations, I have verified that the combination of the proposed size, shape and smoothness terms is suitable for modelling objects of desired shapes. Using the second central moment based shape term, I have shown that the model prefers the formation of elliptical shapes, while the area and perimeter based shape descriptor is more general, and allows us to capture amoeba-like objects.

II/2. I have combined the selective active contour framework with an anisotropic region-based data term. By testing the selective active contour model combined with the region-based data models on a large-scale synthetic data set, I have shown that they are suitable for the size and shape selective segmentation of visual objects. I have tested and demonstrated that the combination of the geometric model and region-based data model is highly robust against image noise.

II/3. By normalizing the components of the energy functional, I have elaborated a more general composite functional. I have approximated the most appropriate theoretical solution, *i.e.* the summation of dimensionless quantities, by normalizing each energy term with a proper function of the desired object size. By testing it on a synthetic data set, I have verified that once the optimal internal weights of the normalized terms are identified, they remain fixed for any object size, whilst maintaining stability. I have successfully applied the selective active contour framework in real biological images for size selective extraction of neuron cells and shape selective segmentation of bacteria.

In the third thesis group, I have presented a new higher-order active contour model for object splitting, called the 'cutting arms' model. The results were published in a conference proceedings [23].

III/1. I have investigated and characterized the desired properties and the shape of the 'cutting arms' higher order active contour model's energy terms, including the functions of curvature, distance and alignment. In order to reduce the necessary calculations, the interactions between point pairs are calculated on a small subset of contour points during the optimization process. Through simulations, I have confirmed that the 'cutting arms' model can efficiently separate single compact objects in object groups. Using a simple pre-segmentation as initialization, I have applied the model on synthetic and real images. I have shown that the general functional of the 'cutting arms' model with special member functions can also provide an object's convex hull.

**Applications** The models of the first thesis group have been successfully used as a starting step of several high-throughput screening related technologies and experiments. The applications of these models were published in three journal papers [19, 20, 21].

| | Publications | | | | | | | |
|---|---|---|---|---|---|---|---|---|
| | [8] | [12] | [13] | [22] | [23] | [19] | [20] | [21] |
| I/1. | • | | | | | | | |
| I/2. | • | | | | | | | |
| I/3. | | • | • | | | | | |
| II/1. | | | | • | | | | |
| II/2. | | | | • | | | | |
| II/3. | | | | • | | | | |
| III/1. | | | | | • | | | |
| Applications | | | | | | • | • | • |

Table 1: The connection between the thesis points, their applications and the Author's publications.

# References

[1] S. Osher and R. P. Fedkiw, *Level set methods and dynamic implicit surfaces*, ser. Applied mathematical sciences. New York, NY, USA: Springer, 2003.

[2] S. Osher and N. Paragios, *Geometric Level Set Methods in Imaging, Vision, and Graphics*. New York, NY, USA: Springer, 2003.

[3] J. A. Sethian, *Level Set Methods and Fast Marching Methods: Evolving Interfaces in Geometry Fluid Mechanics, Computer Vision and Materials Science*. Cambridge, England: Cambridge University Press, 1999.

[4] M. Rochery, I. H. Jermyn, and J. Zerubia, "Higher order active contours," *International Journal of Computer Vision*, vol. 69, no. 1, pp. 27–42, 2006.

[5] P. Horvath, I. H. Jermyn, Z. Kato, and J. Zerubia, "A higher-order active contour model of a 'gas of circles' and its application to tree crown extraction," *Pattern Recognition*, vol. 42, no. 5, pp. 699–709, 2009.

[6] M. Rochery, I. Jermyn, and J. Zerubia, "Phase field models and higher-order active contours," in *Tenth IEEE International Conference on Computer Vision (ICCV'05)*, vol. 2. IEEE, 2005, pp. 970–976.

[7] P. Horváth and I. H. Jermyn, "A gas of circles phase field model and its application to tree crown extraction," in *2007 15th European Signal Processing Conference*. IEEE, 2007, pp. 277–281.

[8] C. Molnar, Z. Kato, and I. Jermyn, "A multi-layer phase field model for extracting multiple near-circular objects," in *Pattern Recognition (ICPR), 2012 21st International Conference on*. IEEE, 2012, pp. 1427–1430.

[9] N. Anastasov, I. Höfig, V. Radulović, S. Ströbel, M. Salomon, J. Lichtenberg *et al.*, "A 3d-microtissue-based phenotypic screening of radiation resistant tumor cells with synchronized chemotherapeutic treatment," *BMC cancer*, vol. 15, no. 1, p. 466, 2015.

[10] J. A. Hickman, R. Graeser, R. de Hoogt, S. Vidic, C. Brito, M. Gutekunst *et al.*, "Three-dimensional models of cancer for pharmacology and cancer cell biology: Capturing tumor complexity in vitro/ex vivo," *Biotechnology journal*, vol. 9, no. 9, pp. 1115–1128, 2014.

[11] M. Nobis, E. J. McGhee, J. P. Morton, J. P. Schwarz, S. A. Karim, J. Quinn *et al.*, "Intravital flim-fret imaging reveals dasatinib-induced spatial control of src in pancreatic cancer," *Cancer research*, vol. 73, no. 15, pp. 4674–86, 2013.

[12] C. Molnar, Z. Kato, and I. H. Jermyn, "A new model for the segmentation of multiple, overlapping, near-circular objects," in *Digital Image Computing: Techniques and Applications (DICTA), 2015 International Conference on*. IEEE, 2015, pp. 1–5.

[13] C. Molnar, I. H. Jermyn, Z. Kato, V. Rahkama, P. Östling, P. Mikkonen *et al.*, "Accurate morphology preserving segmentation of overlapping cells based on active contours," *Scientific reports*, vol. 6, p. 32412, 2016.

[14] D. Zhang and G. Lu, "Review of shape representation and description techniques," *Pattern Recognition*, vol. 37, pp. 1–19, 2004.

[15] D. Mumford, "Elastica and computer vision," in *Algebraic geometry and its applications*. New York, NY, USA: Springer, 1994, pp. 491–506.

[16] T. Chan and L. Vese, "An active contour model without edges," in *International Conference on Scale-Space Theories in Computer Vision*. Springer, 1999, pp. 141–151.

[17] S. Lankton and A. Tannenbaum, "Localizing region-based active contours," *IEEE Transactions on Image Processing*, vol. 17, no. 10, pp. 2029–2039, 2008.

[18] C. Li, C.-Y. Kao, J. C. Gore, and Z. Ding, "Minimization of Region-Scalable Fitting Energy for Image Segmentation," *Image Processing, IEEE Transactions on*, vol. 17, no. 10, pp. 1940–1949, 2008.

[19] J. C. Caicedo, S. Cooper, F. Heigwer, S. Warchal, P. Qiu, C. Molnar *et al.*, "Data-analysis strategies for image-based cell profiling," *Nature methods*, vol. 14, no. 9, p. 849, 2017.

[20] C. Brasko, K. Smith, C. Molnar, N. Farago, L. Hegedus, A. Balind *et al.*, "Intelligent image-based in situ single-cell isolation," *Nature communications*, vol. 9, no. 1, p. 226, 2018.

[21] Z. Farkas, D. Kalapis, Z. Bódi, B. Szamecz, A. Daraba, K. Almási *et al.*, "Hsp70-associated chaperones have a critical role in buffering protein production costs," *eLife*, vol. 7, p. e29845, 2018.

[22] J. Molnar, A. I. Szucs, C. Molnar, and P. Horvath, "Active contours for selective object segmentation," in *Applications of Computer Vision (WACV), 2016 IEEE Winter Conference on.* IEEE, 2016, pp. 1–9.

[23] J. Molnar, C. Molnar, and P. Horvath, "An object splitting model using higher-order active contours for single-cell segmentation," in *International Symposium on Visual Computing.* Springer, 2016, pp. 24–34.